Received: 6 November 2020 | Revised: 17 February 2021 | Accepted: 20 February 2021

DOI: 10.1111/ffe.13442

ORIGINAL CONTRIBUTION

FFEMS Fatigue & Fracture of Engineering Materials & Structures WILEY

On the performance of monopile weldments under service loading conditions and fatigue damage prediction

Romali Biswal[1] | **Abdullah Al Mamun**[2] | **Ali Mehmanparast**[1]

[1]Offshore Renewable Energy Engineering Centre, Cranfield University, Bedford, UK

[2]Department of Mechanical Engineering, University of Bristol, Bristol, UK

Correspondence
Ali Mehmanparast, Offshore Renewable Energy Engineering Centre, Cranfield University, Bedford MK43 0AL, UK.
Email: a.mehmanparast@cranfield.ac.uk

Funding information
Engineering and Physical Sciences Research Council, Grant/Award Number: EP/L016303/1

Abstract

Thick weldments used in offshore structures frequently act as fatigue crack initiation sites due to stress concentration at weld toe as well as weld residual stress fields. This paper investigates the cyclic deformation behavior of S355 G10+M steel, which is predominantly used in offshore wind applications. Owing to the vast size difference of monopile structure and weld cross-section, a global–local finite element (FE) method was used, and the weld geometry was adopted from circumferential weld joints used in offshore wind turbine monopile foundations. Realistic service loads collected using supervisory control and data acquisition (SCADA) and wave buoy techniques were used in the FE model. A nonlinear isotropic–kinematic hardening model was calibrated using the strain controlled cyclic deformation results obtained from base metal (BM) as well as cross-weld specimen tests. The tests revealed that the S355 G10 +M BM and weld metal (WM) undergo continuous cyclic stress relaxation. Fatigue damage over a period of 20 years of operation was predicted using the local stress at the root of the weldments as the life limiting criterion. This study helps in quantifying the level of conservatism in the current monopile design approaches and has implications towards making wind energy more economic.

KEYWORDS

fatigue life prediction, finite element modeling, offshore wind turbine, S355 welds, service loads

1 | INTRODUCTION

Over the last 15 years, constant efforts have been directed towards promoting renewable energy technologies, and the deployment of new offshore wind farms has rapidly accelerated around the world, particularly in Europe. A recent example of such efforts is the new offshore wind farm being constructed by Seimens Gamesa Renewable off the coast of Yorkshire, UK (which is the largest project among the current wind farms) and is approaching completion. It is estimated that by 2024, this wind farm could result in meeting the energy demand of 1.2 million households in the United Kingdom.[1] Nevertheless, being a relatively new technology as compared to fossil fuels, considerable efforts have been put towards bringing down the levelized cost of energy (LCOE) for offshore wind power, which would render the technology commercially competitive.[2,3] It has been established that scaling up the offshore wind turbine (OWT) size, which includes taller mast (thereby giving access to stronger

winds) and larger rotor blades (which increases the swept area), enhances the efficiency but requires advanced designs to withstand greater structural loads.[4]

Steady efforts have been focused towards development of optimized features for rotor blades,[5,6] tower,[7,8] foundation,[9,10] and structural health monitoring.[11,12] In addition to exploring newer methods, many studies have been carried out to enhance the structural integrity of existing designs by studying the strength limitations for S355 and development of numerical models. Jacob et al.[13] investigated the residual stress profile in a typical circumferential butt weld of OWT monopile made of S355 G10+M and found compressive residual stresses in the heat affected zone (HAZ). Since this would lead to a reduction in the value of stress intensity factor (crack driving force), such weld residual stresses would be beneficial in life extension of the OWT. In a numerical study, it was found that peak stress method can be used to calculate the linear notch stress intensity factor under mode I loading, where the weld toe profile is assumed as a sharp, zero-radius V-notch.[14] However, Ferro et al.[15] reported that if the applied stress amplitude (or service load) is such that the local stress at the weld toe (treated as a V-notch) is beyond the elastic limit of the material, the weld residual stresses in the plastic zone would be redistributed in the first loading cycle. Similarly, the interaction of environmental factors with fatigue crack can significantly alter the material behavior.[16] Igwemezie and Mehmanparast[17] studied the impact of loading frequency and waveform of load cycle on the corrosion fatigue process. Experimental work done by Taylor et al.[18] showed that the material parameters such as smaller grain size and higher fracture toughness are favorable for crack initiation but do not correlate to crack arrest, which is also essential to avoid catastrophic failure. Mehmanparast et al.[19] studied the effect of environment (i.e. air and seawater) and microstructure (BM and HAZ) on the fatigue crack growth in S355 G8 +M and reported that in free corrosion condition, the crack growth rate was increased by a factor of 2 as compared to tests conducted in air. Another independent study was conducted by the authors to characterize the mechanical and fracture properties of monopile weldments to improve the structural integrity assessment of monopiles.[20]

Modeling approaches using probabilistic and deterministic methods are widely used to predict fatigue damage in the OWT structure as a result of cyclic loading conditions. For instance, finite element (FE) approach is a powerful numerical method that is used to calculate the weld residual stress as well as the residual stress redistribution with cyclic load applications.[21] Alternatively, a probabilistic framework can be adopted to estimate the fatigue damage parameter such as Smith–Watson–Topper model (more consistent in the high cycle regime), Walker model (where strain is used to compute the damage parameter, and therefore, the model works well in the low cycle regime as well as high cycle regime), energy-based models (where the strain energy density is used to correlate with the fatigue life and can be extended from uniaxial to multiaxial cyclic loading conditions),[22] critical plane-based model proposed by Fatemi and Socie[23] which is applicable to multiaxial loading condition, and Castillo–Canteli model which is a generalized fatigue damage model that can be used for both uniaxial and multiaxial loading conditions.[24]

Foundation structure acts as a life-limiting component for an OWT as it is subjected to a spectrum of structural loads, such as weight of the rotor and nacelle assembly, bending load from wind, wave currents, and vibrations due to rotor blades. Most of the installed OWTs consist of monopile foundations which are built by stacking 3 to 7 m diameter cylindrical sections of 30 to 125 mm thickness and can cost up to 35% of the total set-up cost of an OWT.[25–27] Besides, the circumferential weldments joining the thick monopile sections lead to material property variations at the WM-HAZ-BM interface, which turns into a favorable site for fatigue crack initiation. This is due to the difference in microstructure and chemical segregation as a result of rapid heating and cooling associated with the submerged arc welding process. Kolios et al.[28] performed linear elastic FE analysis on circumferential weldments in OWT monopile structure and observed that depending on the weld quality, the stress concentration factor (SCF) at weld toe lies between 1.1 and 1.65. Subsequent fatigue tests conducted with large scale dog-bone samples extracted from 90 mm thick weldments displayed crack initiation at regions of maximum stress concentration.[28] In Jacob et al.,[29] the authors studied the stress–strain response at the different sections, that is, BM, HAZ, and WM of a cross-weld specimen using digital image correlation technique. It was found that the three regions exhibited comparable values of tensile strength; however, the elongation to failure of the WM and HAZ was reduced by a factor of 10 with respect to the BM. As the OWT weldments are not subjected to any post-weld treatment, a combination of mechanical properties mismatch (between HAZ and the surrounding BM), residual stress, and SCF at weld toe make it a potential site for fatigue crack initiation. Another study[30] used downsized geometries of monopile section to investigate the effect of bending moment. The stresses were found to be greatest at regions nearest to the fixed bottom of the monopile, which in an OWT would be the section just around the sea-bed. However, the loading conditions in an OWT are governed by

multiple factors such as wind (speed and direction), wave (height and frequency), and rotor speed. Therefore, some researchers[26,31,32] used supervisory control and data acquisition (SCADA) technique to measure the true service loads acting on an OWT.

Another form of relevant damage mechanism in OWT structures is due to corrosion. Corrosion-fatigue process is initiated by the formation of localized corrosion pits at certain parts of the wind turbine structure, which are formed as a result of the breakdown of the thin oxide layer on the surface of metals, which then develop into a critical size large enough to initiate a crack. However, the quantification of corrosion-fatigue mechanism poses an important challenge as the pit-to-crack stage of this process is largely unknown; hence, in most instances, the pit itself is often taken as a crack in the fatigue analysis.[17,33,34] Corrosion damage can be accounted for in the fatigue design process by considering the S–N curves for structural steels in seawater with and without cathodic protection.[19] Nevertheless, such a prediction would have inherent uncertainties due to the variations in corrosion rate with geometric location as well as the water depth. This difference is a result of the variations in the chemical composition of the seawater at different locations. Seawater is generally considered to be composed of 3.5 wt.% of sodium chloride (NaCl), and its pH ranges from 7.8 to 8.3.[25] The splash zone (at the free surface of sea) is considered to undergo maximum uniform corrosion that could amount to a yearly thickness reduction of 0.2–0.4 mm in the OWT monopile structure.[33] The submerged sections are subjected to a thickness reduction of 0.1–0.2 mm per year.[33]

The present study aims to analyze the effect of service loading conditions on offshore wind monopile foundation structure using a full scaled FE model to predict the fatigue life of the structure. A global–local model was used to enable optimized computation of local stress and strain value at the weld toe of circumferential butt weld joints located nearest to the sea-bed. The model was calibrated using strain controlled cyclic test data to improve the prediction accuracy. Development of reliable fatigue life prediction tools will encourage design optimizations on OWT structures and therefore make wind energy harvesting more economic.

2 | MATERIAL AND TEST METHODS

The material considered in this study is S355 G10+M structural steel since it is commonly employed in fabrication of OWT foundation structures. In S355 G10+M notation, the letter S indicates that the material is a structural steel with a minimum yield stress of 355 MPa, G10 indicates the steel grade within the material groups specified in EN-10225 standard, and +M indicates thermo-mechanical rolling process. A 90 mm-thick hot rolled plate was welded using submerged arc welding process, and three circular round bar specimens were extracted from the weld region as shown in Figure 1A, referred to as cross-weld specimens. Details of the welding procedure can be found in a previous study by Jacob et al.[29] The specimen extraction location was selected such that the 2- to 3-mm-thick HAZ was positioned at the center of the specimen gage section. This configuration allows the interface between WM, HAZ, and BM to be tested under the applied loading condition. Therefore, the test results obtained from the cross-weld specimens would represent the material behavior of the circumferential weldments in OWT monopile structures. Further, three more specimens were extracted from the 90-mm-thick hot rolled plate (i.e., without any weldment) to represent the BM material properties. All the specimens were designed according to ASTM E606 design standard[35] as shown in Figure 1B.

Strain-controlled cyclic load tests were performed using a 100-kN Instron servo-hydraulic machine at room temperature condition. The strain value was measured using an Instron extensometer attached to the gage section of the specimen through a spring and tension string combination. The measurement frequency was set at 40 Hz to capture 400 data points every cycle. Three strain amplitudes of ±1%, ±2%, and 0–3% were selected to capture the cyclic deformation behavior of the cross-weld and BM specimens. Two tests were performed at each strain amplitude, with one test capturing the cross-weld material behavior while the second test giving the BM performance that was treated as a reference for comparison purposes. In each test, the specimen was loaded at a frequency of 0.1 Hz. The tests were conducted for 200 cycles or until failure, if the cycles to failure were less than 200 cycles.

For the purpose of determining the service loads acting on an OWT, online monitoring data for the wind and wave characteristics were taken from an offshore wind farm located in the North Sea. The data were collected from a 6-MW capacity OWT which had a rotor diameter of 154 m and hub height of 106 m. The measurement and recording of the wind profile were carried out using SCADA system. The data were collected for a period of 2 years, from beginning of 2016 to the end of 2017. The data included main shaft rotational frequency (RPM), wind speed (minimum, maximum, mean, and standard deviation), wind direction (monitored by the yaw position sensor), ambient temperature, and turbine power generation, recorded every 10 min over the 2-year

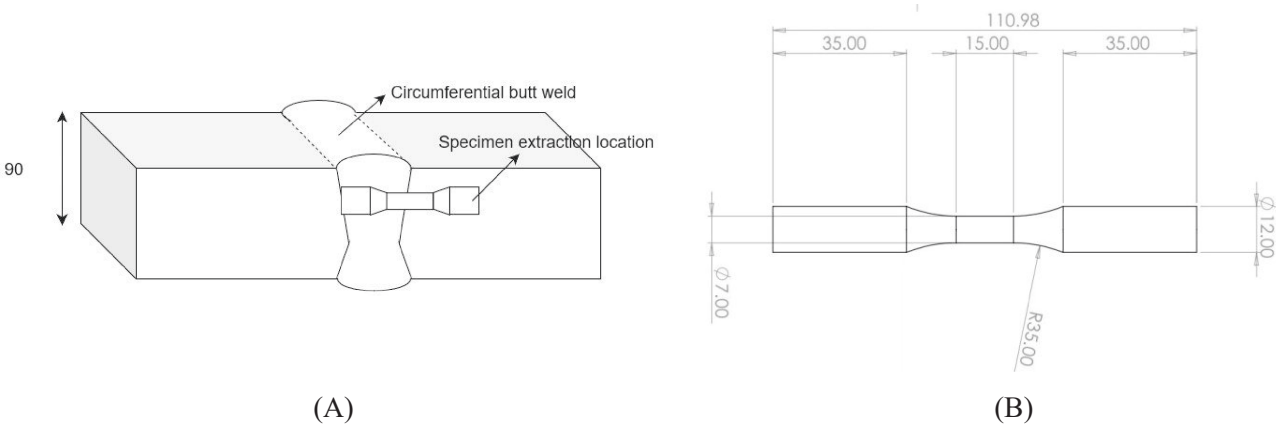

FIGURE 1 Schematic showing (A) extraction location for preparing cross-weld specimens and (B) specimen geometry (all dimensions are in millimeters)

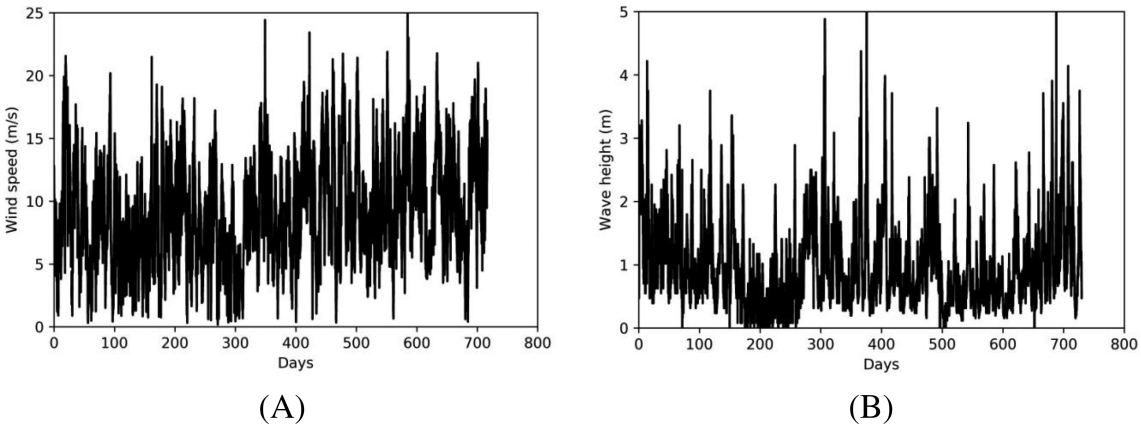

FIGURE 2 Two years of online monitoring data showing variation of (A) wind speeds and (B) wave heights

duration. Similarly, the wave characteristics including the maximum wave height, wave period, mean wave spectral direction, and water temperature were monitored using a wave buoy (SEAWATCH midi model) at an interval of every 30 min over the 2-year period. The wind speed and wave height variations exhibited a random behavior with respect to time as shown in Figure 2A,B, respectively.

The variation of the wave speed along the depth of the sea was also monitored by taking measurements every 3 m from the free surface of seawater, up to a depth of 33 m below the sea level. Figure 3 shows that the wave speed below the sea level remains fairly constant with increasing depth and undergoes a rapid drop as the depth reaches 24 m. This value corresponds to a region within few meters of sea floor, and the fall in wave speed can be explained by the obstruction offered by the seabed. It is worth mentioning that this measurement indicates that the sea waves at the sea level would have maximum contribution towards wave loads; therefore, the present study uses the height of sea waves at the surface to compute the wave loads on the monopile foundation.

3 | MODELING METHODOLOGY

3.1 | Determination of service loads on OWT monopile structure

3.1.1 | Hydrodynamic forces due to sea waves

As Figure 2B denotes, the waves can vary over a wide spectrum of heights and periods which are nonlinear and stochastic. For modeling purpose, a linear wave theory was adopted to represent the sea waves. Morison's semi-empirical equations[36] give the hydrodynamic forces due to an unsteady, viscous flow acting on a fixed body along the flow (i.e., wave) direction. The total hydrodynamic force is composed of two components in this study as

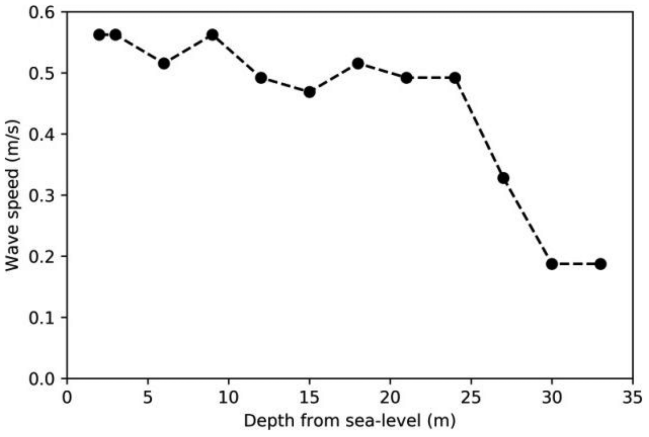

FIGURE 3 Variation of speed of waves with increasing depth from free surface of sea

shown in Equation 1. The first term represents the inertia force due to acceleration of the surrounding fluid while the second term gives the contribution of the viscous drag force against the monopile surface. Therefore, Morison's approach was used in this study with the following critical assumptions:

1. The wave flow is irrotational and incompressible; that is, vorticity is zero for the flow. With this assumption, a scalar potential function can be used to represent the hydrodynamic flow.
2. The seabed is horizontal, impermeable, and provides a fixed support to the monopile structure; that is, the soil–monopile interaction was neglected in this study.
3. Pressure at the sea surface is constant.
4. Force acting on the structure due to undisturbed waves is negligible.
5. Wave diffraction and wave splash on the monopile surface are negligible (due to the large monopile size considered in this study).
6. The mass coefficient and drag coefficient remain constant throughout the service life. This assumption is used to make the computation easier.

From Figures 2B and 3, it is evident that wave speed coming across on a monopile section varies with time and depth. Equation 1 shows the force acting on an infinitesimal section of the monopile due to the waves. The total force on a monopile structure due to sea waves was therefore evaluated using an integration shown in Equation 2.

$$dF(z,t) = C_m \frac{\rho \pi d^2}{4} u(z,t)dz + C_d \frac{\rho d}{2} u(z,t)|u(z,t)|dz \quad (1)$$

$$F(z,t) = \int_{z=0}^{z=L} dF(z,t) \quad (2)$$

where C_m and C_d are the coefficients of inertia force (referred to as mass coefficient) and viscous drag force (referred to as drag coefficient), respectively. In the present study, the values of C_m and C_d were assumed to be 2 and 0.7.[36] The remaining terms are density of seawater ρ, diameter of monopile structure d, wave speed u which is a function of height from sea-floor z, and time t. The length of submerged section of the monopile structure is L.

Following this, the wave speed variation recorded over the 2 years of online monitoring was sorted into six groups using the rainflow counting algorithm[37] implemented in MATLAB. Also, the frequency of occurrence of these wave speeds over the 2-year period was used to estimate the weight that should be given to each group during fatigue life analysis. For any given moment in time, one of the load cases (or wave force) and its corresponding frequency were assumed to be acting on the OWT structure.[33]

3.1.2 | Aerodynamic forces due to wind

The classical blade element momentum (BEM) approach[38] was used to compute the loads acting on the rotor due to coursing wind. The wind behavior was modeled with a one-dimensional wave theory. Equations 3 and 4 give the lift and drag forces, respectively, experienced by an airfoil.

$$F_L = \frac{1}{2} C_L \rho V_0^2 c \quad (3)$$

$$F_D = \frac{1}{2} C_D \rho V_0^2 c \quad (4)$$

where C_L and C_D are the coefficients of lift and drag, respectively. The density of air is given by ρ, wind speed V_0, and length of airfoil c. For the purpose of simplicity, an average angle of attack was assumed at 30°, and the corresponding values of C_L and C_D were taken as 0.97 and 0.63 for the calculations.[38]

The total thrust acting on an infinitesimal section of rotor blade is given by Equation 5. Similarly, the moment produced by the incoming wind on an infinitesimal section of the rotor blade is given by Equation 6. The total thrust and moment due to the wind were therefore computed by integrating Equations 5 and 6 over the entire rotor blade. Details of the derivation of the BEM equations can be found elsewhere.[38]

$$dT = \frac{1}{2}\rho B \frac{V_0^2(1-a)^2}{\sin\phi} c C_N \, dr \tag{5}$$

$$dM = \frac{1}{2}\rho B \frac{V_0(1-a)r\omega(1+a')}{\sin\phi\cos\phi} c C_T \, rdr \tag{6}$$

where B is the number of rotor blades in the turbine, a the axial induction factor, a' the factor to account for any rotational speed in the wake (nonideal rotor condition), ϕ the flow angle of incoming wind, C_N the coefficient of normal component of force, r the radial distance from center of rotation of rotor blades, ω the rotational speed of rotor, and C_T the coefficient of tangential component of force.

In order to calculate the wind load, the wind velocity profile was regrouped into six categories using rainflow counting algorithm[37] and implemented in MATLAB. Each group of wind speed was characterized by the frequency of occurrence through the 2 years of monitoring. For each group of wind speed, the mean wind speed of the group was used to calculate the corresponding wind loads using Equations 5 and 6. For any given moment in time, one of the load case (or wind speed and its corresponding frequency) was assumed to be acting on the OWT structure.[33]

3.2 | FE modeling

3.2.1 | Material model

The elastic properties used in the FE model were taken from a previous study as shown in Figure 4A.[29] It can be seen that the tensile strength of the three regions is comparable in Figure 4A; however, the strain to failure shows a significant difference. It is worth mentioning that due to SCF, the stress values at the weld toe may exceed the yield point. Therefore, it is important to use the true material properties while performing a fatigue analysis as ductility plays an important role when the local stresses approach the yield strength of the material. Further, the

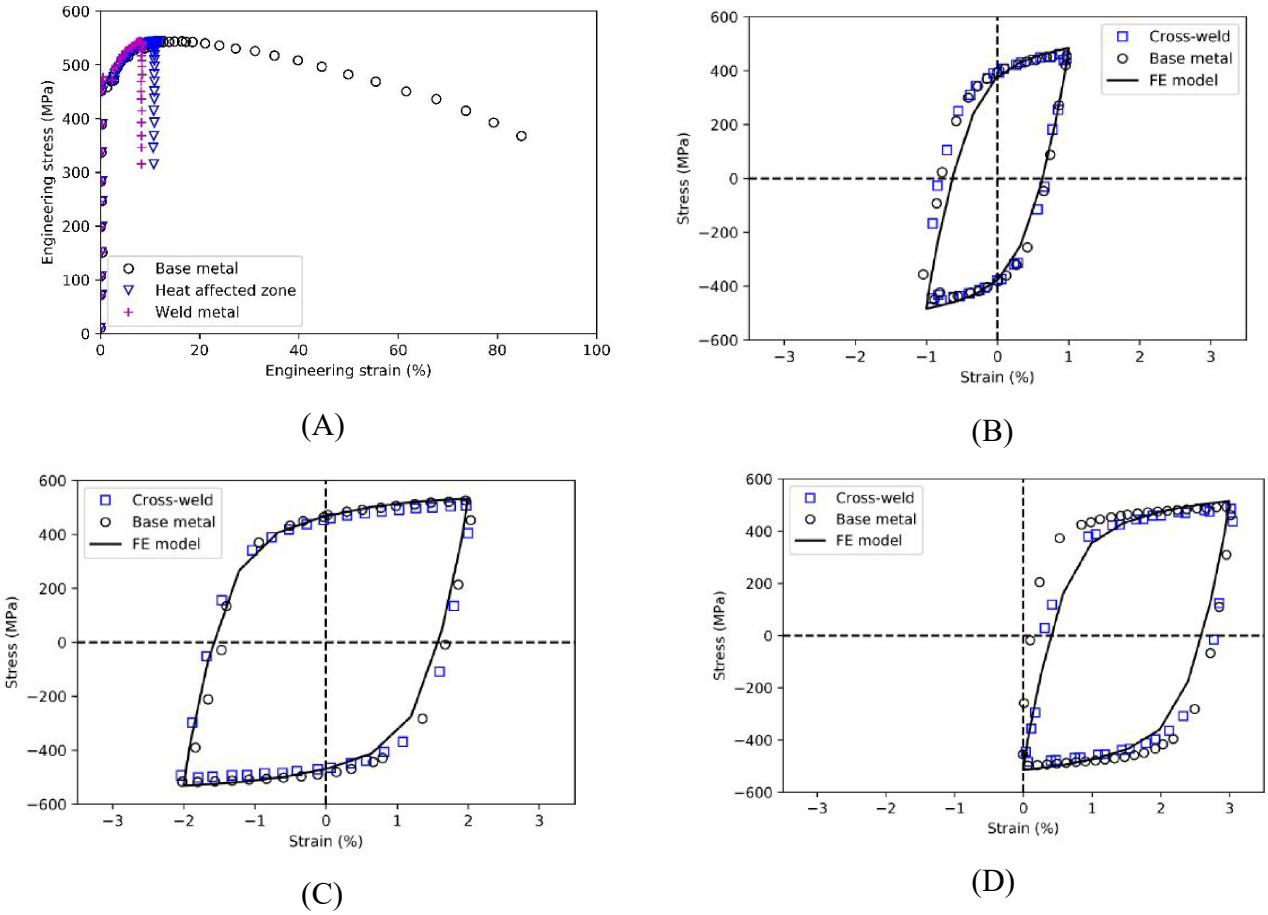

FIGURE 4 Results of strain controlled cyclic load tests showing the stabilized hysteresis loops for cross-weld samples and BM samples tested at (A) ±1% strain, (B) ±2% strain, and (C) 0–3% strain [Colour figure can be viewed at wileyonlinelibrary.com]

stabilized hysteresis loop has been obtained from the cyclic load tests conducted in this study. The tests were performed on the BM and cross-weld specimens as shown in Figure 4B–D. The experimentally measured values of the tensile and cyclic properties of S355 G10+M are given in Table 1. Following this, an elastic–plastic constitutive equation was used to simulate the experimental results. Equation 7 gives the back-stress function which is used to model the kinematic component (i.e., change in the origin of the yield surface in the stress space) of the cyclic softening behavior, and Equation 8 gives isotropic softening component that is the change in the size of the yield surface.

$$\alpha_k = \frac{C_k}{\gamma_k}\left(1 - e^{-\gamma_k \varepsilon^{pl}}\right) + \alpha_{k,1} e^{-\gamma_k \varepsilon^{pl}} \tag{7}$$

$$\sigma^0 = \sigma_0 + Q_\infty \left(1 - e^{-b\bar{\varepsilon}^{pl}}\right) \tag{8}$$

where C_k is the plasticity modulus and γ_k the rate of change in C_k with increase in the applied plastic strain. Similarly, Q_∞ is the change in yield surface with increasing equivalent plastic strain and the rate of change is controlled by the parameter b. The mixed kinematic (C_k [MPa], γ_k) and isotropic (Q_∞ [MPa], b) model parameters fitted to stabilized hysteresis loops (refer Figure 4) for S355 G10+M obtained from cyclic load test. Calibrated parameters for the mixed isotropic–kinematic model are given in Table 1. Five back-stress components were used to improve the fitting of stress–strain response of the model to the experimentally determined cyclic stress–strain response. For each strain range, the back-stress as obtained by integrating Equation 7 over the monotonically rising section of the stabilized hysteresis loop.

Materials exhibiting increasing resistance to plastic deformation with plastic straining can be modeled with an isotropic hardening algorithm. However, the cyclic load test data shown in Figure 4B–D clearly indicate that the elastic yield limit varies in the forward and reverse loading cycles; that is, S355 shows Bauschinger effect. Since Bauschinger effect can be accounted by a kinematic hardening rule, a mixed isotropic–kinematic constitutive model was employed in this study. Further details of the model can be found in the Abaqus manual.[39] In the cyclic load test, it was observed that the stress versus strain response (hysteresis loops) was stabilized within the first 20 cycles; nevertheless, the experiment was conducted for 200 cycles (or until failure if cycles to failure were less than 200). Therefore, the 20th cycle from test was used to calibrate the model, where the set parameters resulted in a good fit between the stress versus strain response of the test and FE model in 20 cycles. Figure 4B–D shows the stabilized cyclic stress versus strain response obtained for the 20th cycle from experiment as well as the FE model.

3.2.2 | Loads and boundary conditions

A three-dimensional FE model was used to determine the peak stresses in the monopile foundation. The separation between two consecutive circumferential welds in the monopile was assumed to be 6.5 m, and the first weld close to the mudline was assumed to be 4 m above the seabed. Since the bending stresses on the monopile decrease rapidly with increasing distance from the fixed end, only the first weld (assumed at 4 m from mudline) was modeled in the FE geometry. Figure 5 shows the FE model dimensions and weld geometry details. It is worth mentioning that the bottom most weld which lies closest to the fixed end of the monopile (buried in the seabed) is subjected to the maximum bending moment. Therefore, this weldment is at the most critical location and has been considered in the FE model. The remaining weldments (shown in dotted lines in Figure 5) have not been included in this study as the separation between the welds is large enough to cause any interaction between the successive welds. Additionally, the regions of load application are also included in the figure, and the corresponding values are summarized in Table 2. As discussed in the previous sections, the loads corresponding to each of the six load cases were applied to determine the maximum stress in the structure. The hydrodynamic and aerodynamic forces for the mean wave height and mean wind speed of each group were calculated from Sections 3.1.1 and 3.1.2, respectively. The following

TABLE 1 Tensile properties of S355 G10+M from literature[29] and calibrated parameters for the cyclic deformation (C_k, γ_k, Q_∞, b) obtained in this study

Monotonic properties				**E**	**ν**	**$\sigma_{0.2(BM)}$**	**$\sigma_{0.2(HAZ)}$**	**$\sigma_{0.2(WM)}$**	**$\varepsilon_{f(BM)}$**	**$\varepsilon_{f(HAZ)}$**	**$\varepsilon_{f(WM)}$**
				196	**0.3**	**455**	**469**	**477**	**87.9**	**10.76**	**8.19**
C_1	γ_1	C_2	γ_2	C_3	γ_3	C_4	γ_4	C_5	γ_5	Q_∞	b
204	9500	120	600	45	565	30	420	12	85	−300	25

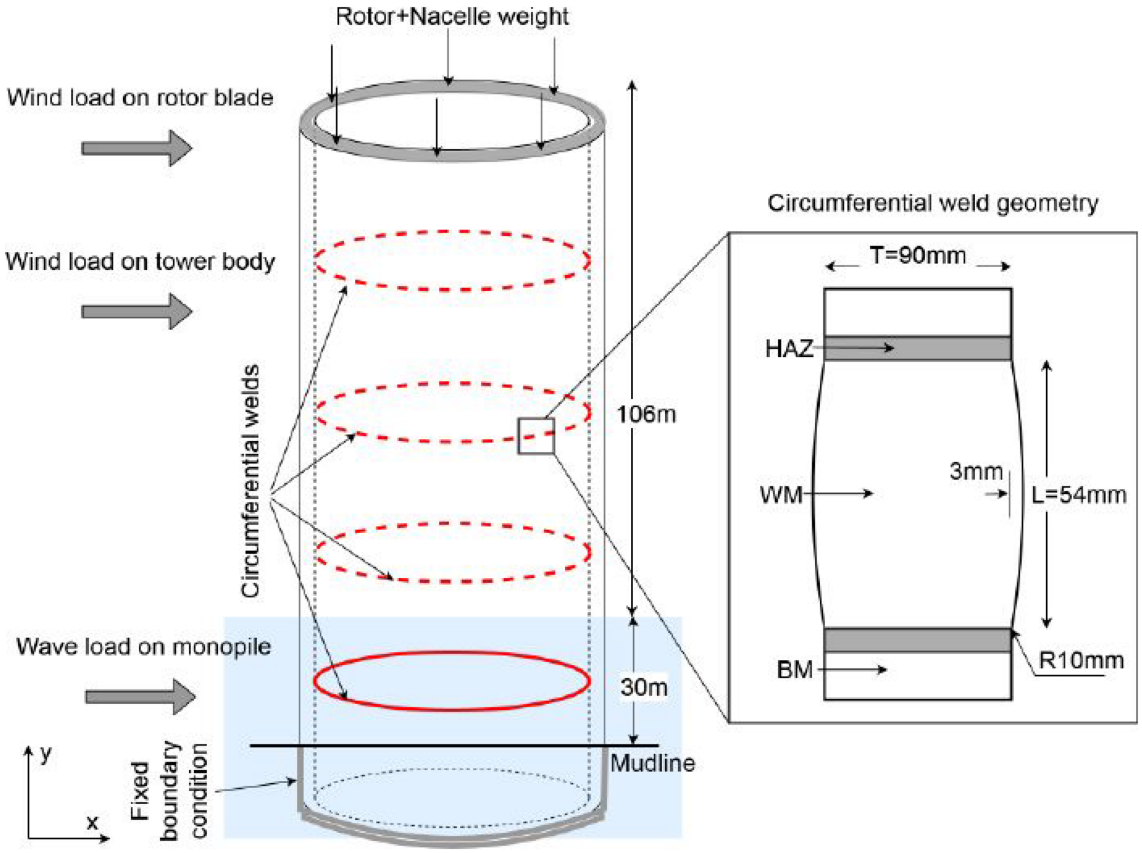

FIGURE 5 Schematic of the model geometry and loading conditions. The weld geometry is shown in the enlarged view on the right. Only the bottom weld (shown in solid red line) was included in the model. (Note: Figure is not to scale. HAZ: heat affected zone, WM: weld metal, BM: base metal) [Colour figure can be viewed at wileyonlinelibrary.com]

TABLE 2 Aerodynamic and hydrodynamic load cases used in the FE model

			Wind load (kN)		Frequency	Wave load (kN)		Frequency
Load case	**Load case probability**	**Cycles**	**Blade**	**Tower**	**(Hz)**	**Inertia**	**Drag**	**(Hz)**
1	0.6119	1,286,459	217	2	0.0275	190	1	0.225
2	0.2986	627,777	515	12	0.0225	462	6	0.2
3	0.0733	154,106	826	32	0.0175	773	17	0.175
4	0.0145	30,485	1145	61	0.0125	1067	38	0.15
5	0.0017	3574	1466	100	0.0075	1343	72	0.13
6	0.0001	210	1769	145	0.0035	1483	105	0.12

regions were selected to apply the corresponding loads as shown in Figure 5:

1. Center of buoyancy of the submerged section of the monopile was used to apply the wave load. This assumption was based on the wave buoy measurements which showed the variation of wave speed with increasing depth of water (refer to Figure 3). It can be seen that the wave speed did not vary significantly for most part of the submerged section. Therefore, the center of buoyancy of the submerged section acts as a suitable point for the wave load application.
2. The wind velocity profile is known to have highest magnitude at the top and decreases rapidly with altitude. However, in the present study, the entire wind profile was not recorded; instead, it was only measured with sensors mounted on the rotor hub. Therefore, the variation of wind load with altitude was neglected, and the centroid of the monopile which was above the water was used as the loading

point for the horizontal wind load acting on the body of the OWT.

3. The majority of the wind load acts on the rotor blades and is transmitted to the OWT structure as a horizontal bending load acting at the top edge of the structure. As the rotor hub assembly was not included in the present model, the wind load on the rotor blades was applied to the top edge of the OWT. It should be mentioned that, in order to avoid singularity, a 100-mm region at the top edge was subjected to tie constraint in ABAQUS, and the horizontal wind load was applied to the tied segment.
4. Structural weight consisting of the rotor and nacelle was applied vertically to the top edge of the tower.

Owing to the large difference between the dimensions of the turbine and the circumferential weldments, a global–local FE model was used in this study. However, the mesh convergence study in the global and local model was conducted for a stress concentration of 1.18 at the weld toe. This value lies in the range of expected SCF values for the OWT weldments. It should be mentioned that FE model aims at determining the effect of the service loads on the OWT weldment; the large difference in the dimension of the features (monopile diameter, plate thickness, and weldment size) limited the minimum element size that could be used while maintaining computation efficiency as well as element aspect ratio for the individual features, particularly the weldment. The global FE model was meshed with elements of sizes varying between 0.5 and 0.1 m, where the mesh was refined at regions closer to the weldment to keep the element aspect ratio within 0.1. The element size in the local model was further reduced between 3 and 20 mm as shown in Figure 6. A 20-noded quadratic hexahedral (brick) element with reduced integration (C3D20R) was used to avoid shear locking phenomenon encountered during bending. In the global model, two elements were used across the thickness of the cylinder so that the total number of elements in the geometry was 10,340. In order to improve the accuracy in the local model, the same was increased to five elements in the local model, thereby resulting in 61,500 elements.

4 | RESULTS AND DISCUSSION

The strain-controlled cyclic test results showed that the load carrying capacity of the cross-weld specimen was comparable to that of the BM. Static test results in the literature[29] presented in Table 1 showed that the strengths of WM and HAZ were both slightly higher than the BM, but such behavior was not noticed in the cyclic test performed in this study. This can be explained by the cyclic softening behavior (Figure 7) observed within the first 20 cycles in this study. Strain-controlled test leads to

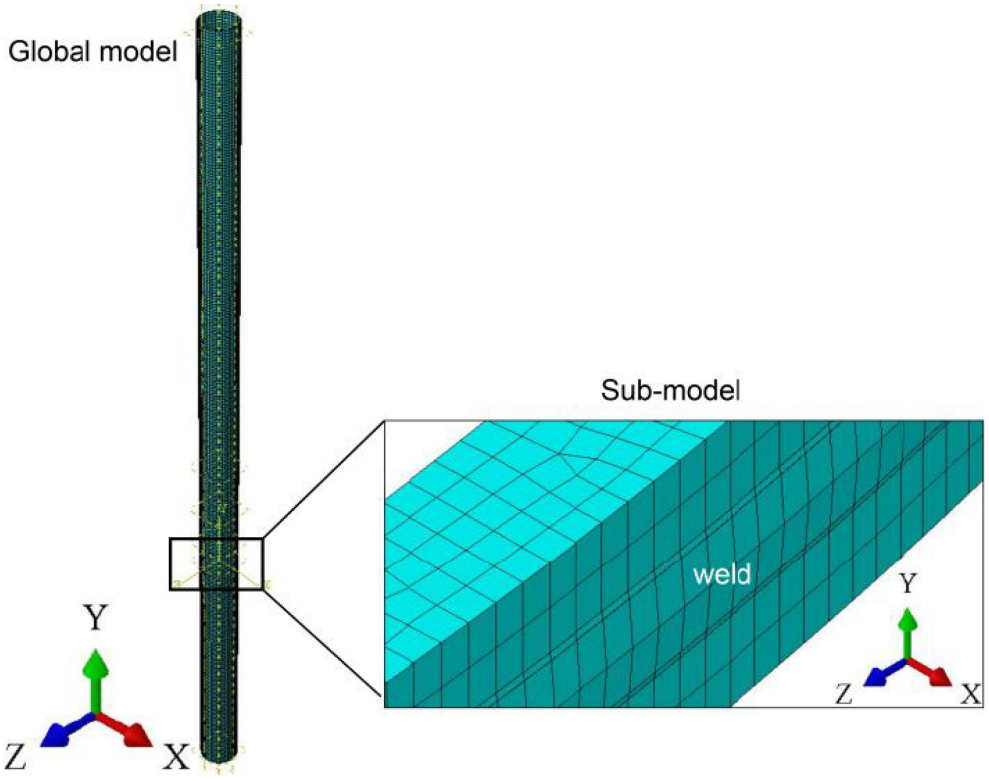

FIGURE 6 FE model mesh showing the two-step modeling approach: Stress distribution from global model was applied as boundary condition in the local model at the weldment [Colour figure can be viewed at wileyonlinelibrary.com]

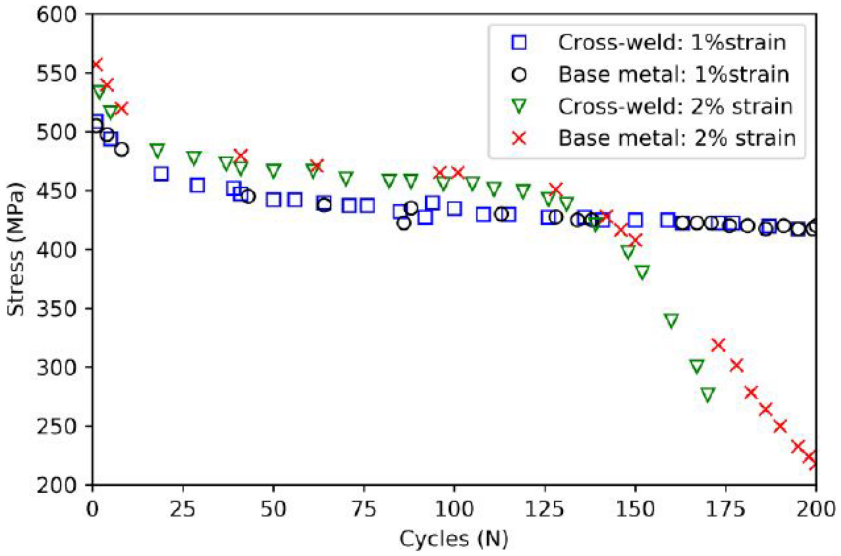

FIGURE 7 Cyclic softening response of S355 G10+M under strain-controlled loading condition obtained from the test [Colour figure can be viewed at wileyonlinelibrary.com]

application of plastic strains to the material; that is, the material is deformed well beyond the yield strength. Since a stress plateau region is characteristic of metals due to work hardening, the difference in the behavior of the cross-weld specimen and BM specimen becomes negligible. Moreover, the application of cyclic loads causes the stress to relax in consecutive cycles owing to the Bauschinger effect. Therefore, the experimental results obtained from this study indicate that the cyclic deformation behavior of circumferential welds employed in OWT structures can be predicted using the BM material properties.

The peak local stress values in the OWT structure were obtained from FE analysis, and the results are shown in Figure 8. As seen in Figure 8B, the higher stress values were found near the weld toe with lower values found further away from the weld region. Also seen in this figure is that the maximum stress values at the weld toe were below the yield stress of the material, indicating zero or limited plastic deformation during the operational life of the OWT monopile. The deformation in the OWT caused bending stresses; therefore, the stress at the weld toe was compared to a nearby region instead of the nominal stress further away. Further, the discontinuity between stress values is observed (Figure 8B) at the junction due to the change in section thickness, that is, weld profile. Since the weld geometry was included in the model, the effect of stress concentration at the weldment has been considered. It should be mentioned that the weld geometry used in the FE analysis was taken from literature where S355 welds were performed on 90-mm-thick plates as considered in this study.[19] The SCF for the chosen weld geometry was found to be 1.18, which falls between the values reported by Kolios et al.[28] The maximum stress produced at the weld toe of the circumferential weld in the monopile was fully reversed; that is, mean stress was zero. Assuming that the weld is free from any residual stresses, a null mean stress condition would indicate that the structure will have better resistance to fatigue crack growth since only half of the cycle (when stress is tensile in nature) can contribute towards fatigue crack growth. For all the six load cases (refer Table 2 for values), the stress versus strain curve showed elastic behavior similar to that of shown in Figure 8C. This suggests that the stresses in the monopile are well within the design criterion, and the S–N fatigue design life approach can be employed to estimate the remaining life of the service exposed monopile. However, this study has not taken the effect of residual stress and environment interaction which can have significant effects on the result. Further, the calibrated material model's contribution was negligible since the stress values were found to be within the elastic regime of the material. However, the proposed cyclic plasticity material model would be useful for applications looking into the effect of hammering loads on the monopile during the installation process in future work as well as the fatigue life assessment in the case of storm events (i.e., over loads).

Figure 9A shows the maximum stress and strain values for the respective load cases obtained from the FE model. The selected weld geometry showed a stress concentration value of 1.18, but it is worth mentioning that depending on the weld profile, the SCF for OWT weldments is reported to vary between 1.1 and 1.6.[28] Therefore, according to the DNVGL-RP-C203 standard[40] (Equation 7 for as welded joints in free corrosion environment which is referred to as D curve), the number of fatigue cycles to failure corresponding to each load case was determined.

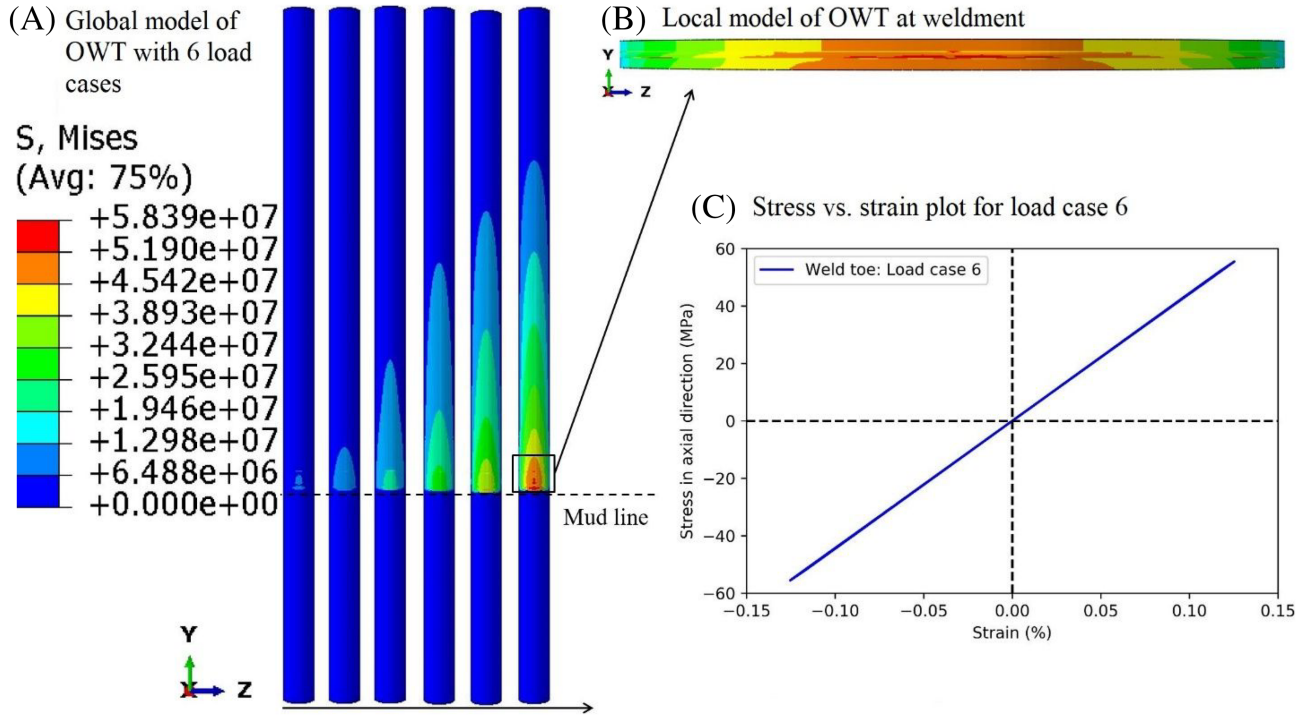

FIGURE 8 (A) von Mises stress profile in the OWT structure obtained for the six load cases from Table 2, (B) submodel result for load case 6 to highlight the local stress concentration at the weld toe, (C) axial stress (in *y*-direction) versus axial strain variation at the weld toe for the (cyclic) load case 6 [Colour figure can be viewed at wileyonlinelibrary.com]

$$\log N_i = 11.687 - 3\log\left(\Delta\sigma_i\left(\frac{t}{t_{ref}}\right)^{0.2}\right) \tag{9}$$

where $\Delta\sigma_i$ is the stress range corresponding to which the cycles to failure N_i are calculated. Further, the monopile structure in this study consists of a weldment of 90-mm thickness; therefore, a thickness correction is applied according to the guidelines provided in DNVGL-RP-C203 standard such that t_{ref} denotes a thickness of 25 mm and t is the corrected weld thickness. Since the plate thickness and weld width both affect the local stress field at the weld toe, the effective thickness of the plate was given by Equation 8. For the weld geometry considered in this study, the values of plate thickness T and weld width L are 90 and 54 mm, respectively, as shown in Figure 5.

$$t = \min[(14mm + 0.66L), T] \tag{10}$$

$$D = \sum_{n=1}^{6} \frac{n_i}{N_i} \tag{11}$$

Following this, the damage D for each load case was calculated using Palmgren–Miner method as shown in Equation 11. Depending on the load case probability given by the rainflow algorithm in Table 2, the number of fatigue cycles to which the monopile structure is subjected to over a period of 20 years (n_i) was calculated. Since the wind and wave characteristics were measured for a period of 2 years, it was assumed that similar characteristics are applicable for a period of 20 years, which is the design life of the OWT structure. Subsequently, the number of fatigue cycles to failure (N_i) was calculated from the stress-life equation given in Equation 7. Figure 9B shows the number of fatigue cycles sustained by the OWT in the 20 years of operation (n_i) and the number of cycles that the structural material (S355) can withstand before fatigue failure occurs (N_i). Figure 9C shows that at the end of 20 years, the total fatigue damage in the monopile structure caused due to all the load cases is well within the design limits, and the cumulative damage value was found to be 7.13%. This shows a sufficiently large safety margin against failure. It is worth noting that the present study has been conducted on a monopile weldment geometry with a relatively low SCF as the weld toe and in the absence of welding residual stresses. Therefore, further studies will be conducted in future work to account for the variation in SCFs as well as the residual stress profiles to provide a better

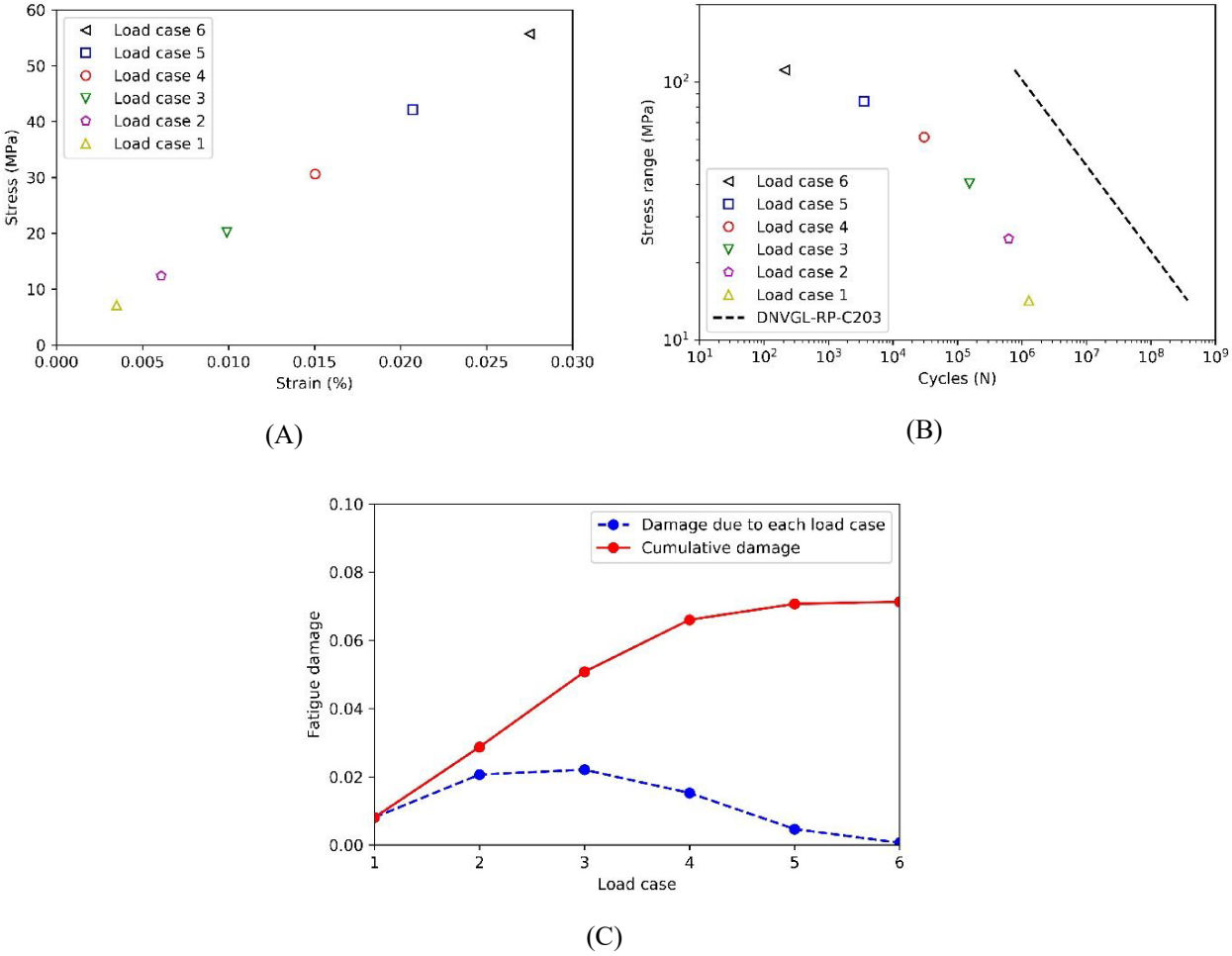

FIGURE 9 (A) Maximum stress and strain values for the respective load cases obtained from the FE model, (B) fatigue cycles sustained by OWT in 20 years (n_i: marker points) and cycles that S355 can withstand before fatigue failure (N_i: dotted line), and (C) fatigue damage caused by individual load cases and cumulative fatigue damage according to Minor's method [Colour figure can be viewed at wileyonlinelibrary.com]

estimation of the OWT monopile fatigue life under realistic operational loading conditions.

This study found that the presently followed design criterion is leading to overdesigning of the OWT structure, thereby adding to the capital expenditure (CAPEX) cost and impacting the commercial aspect of the wind energy production. The maximum stress and strain in the structure were found to be within the elastic regime of S355 G10+M. Plastic deformation was not observed for any of the load cases, therefore indicating that the monotonic properties of the material are sufficient for determining the design limits. The cyclic deformation behavior of S355 G10+M was studied experimentally as it is widely used in a number of structural applications and can be used to investigate the effect of over loads on the structure. Further, the proposed parameters for the cyclic deformation analysis using FE method will be useful for over load analysis.

5 | CONCLUSIONS AND FUTURE WORK

In this study, the fatigue damage in an OWT under service loading conditions was investigated. The online monitoring data collected for two continuous years from an offshore wind farm in the North Sea using SCADA and wave buoy were presented, and a MATLAB code was used to implement rainflow cycle counting technique to analyze the wind and wave parameters. Further, Morison's semi-empirical equations and BEM equations were solved to compute the cyclic loads (frequency, amplitude, and mean value). The data from the 2-year period were assumed to be representative of the entire service life (i.e., 20 years) of the OWT, and subsequently, six load cases were identified and applied in ABAQUS software to determine the maximum stress induced in the OWT structure. Additionally, the material (S355 G10 +M) was tested under strain-controlled cyclic loading to

determine the material behavior for low cycle fatigue regime. Subsequently, a cyclic plastic constitutive model (mixed isotropic–kinematic) was used in the FE analysis. For each load case, the fatigue damage over a period of 20 years of operation was estimated using Miner's criterion. The findings can be summarized as follows:

1. Strain-controlled cyclic load testing of S355 showed the cyclic softening behavior with a 10% drop in stress level in the stabilized hysteresis loop for all the tested strain amplitudes.
2. The fatigue damage was found be greatest for the load cases with stress magnitudes below 25 MPa, that is, load cases 1–3. Therefore, it can be concluded that for OWT applications, instead of stress amplitude, the frequency plays a significant role in the fatigue damage.
3. A nonlinear constitutive equation was proposed to model the cyclic deformation behavior of S355 for large strain applications (up to 3% strain). However, the present study showed that the peak stress and strain values in the structure were within the elastic regime.
4. The cumulative fatigue damage calculated for the OWT monopile was 7.13% after 20 years of operation under the realistic service loads. This indicates that the structural design can be optimized for reducing the material cost, thereby making wind power generation more economic.

Although the present study concluded that the stress magnitudes induced in an OWT monopile structure are well within the elastic limit of the material, this may not be true for the bigger and more complex designs of OWT structures which are being explored for floating OWTs. The use of in-service load history gives realistic loading conditions and therefore improves the prediction models.

ACKNOWLEDGMENTS

This work was supported by grant EP/L016303/1 for Cranfield, Oxford and Strathclyde Universities, Centre for Doctoral Training in Renewable Energy Marine Structures—REMS from the U.K. Engineering and Physical Sciences Research Council (EPSRC).

DATA AVAILABILITY STATEMENT

The datasets generated during and/or analyzed during the current study are available from the corresponding author on request.

NOMENCLATURE

BM	base metal
DNV	Det Norske Veritas
E	Young's modulus
FEA	finite element analysis
HAZ	heat affected zone
LCOE	levelized cost of energy
OWT	offshore wind turbine
SCADA	supervisory control and data acquisition
SCF	stress concentration factor
ν	Poisson's ratio
WM	weld metal
wt.%	weight percent

ORCID

Ali Mehmanparast https://orcid.org/0000-0002-7099-7956

REFERENCES

1. Dorrell G, Díaz V. Siemens Gamesa's flagship 14 MW turbine to power 1.4 GW Sofia offshore wind power project in the UK. Siemens Gamesa. *Renew Energy*. 2020.
2. Johnston B, Foley A, Doran J, Littler T. Levelised cost of energy, A Challenge for Offshore Wind. *Renew Energy*. 2020; 160:876-885. https://doi.org/10.1016/j.renene.2020.06.030
3. Sharifzadeh M, Lubiano-Walochik H, Shah N. Integrated renewable electricity generation considering uncertainties: the UK roadmap to 50% power generation from wind and solar energies. *Renew Sustain Energy Rev*. 2017;72:385-398. https://doi.org/10.1016/j.rser.2017.01.069
4. Barutha P, Nahvi A, Cai B, Jeong HD, Sritharan S. Evaluating commercial feasibility of a new tall wind tower design concept using a stochastic levelized cost of energy model. *J Clean Prod*. 2019;240:118001. https://doi.org/10.1016/j.jclepro.2019.118001
5. MacPhee DW, Beyene A. Experimental and fluid structure interaction analysis of a morphing wind turbine rotor. *Energy*. 2015;90:1055-1065. https://doi.org/10.1016/j.energy.2015.08.016
6. Regodeseves PG, Morros CS. Unsteady numerical investigation of the full geometry of a horizontal axis wind turbine: flow through the rotor and wake. *Energy*. 2020;202:117674. https://doi.org/10.1016/j.energy.2020.117674
7. Jin Q, Li VC. Structural and durability assessment of ECC/concrete dual-layer system for tall wind turbine towers. *Eng Struct*. 2019;196:109338. https://doi.org/10.1016/j.engstruct.2019.109338
8. Yadav KK, Gerasimidis S. Imperfection insensitive thin cylindrical shells for next generation wind turbine towers. *J Constr Steel Res*. 2020;172:106228. https://doi.org/10.1016/j.jcsr.2020.106228
9. Lin K, Xiao S, Zhou A, Liu H. Experimental study on long-term performance of monopile-supported wind turbines (MWTs) in sand by using wind tunnel. *Renew Energy*. 2020;159:1199-1214. https://doi.org/10.1016/j.renene.2020.06.034
10. Ma H, Yang J. A novel hybrid monopile foundation for offshore wind turbines. *Ocean Eng*. 2020;198:106963. https://doi.org/10.1016/j.oceaneng.2020.106963
11. Long L, Mai QA, Morato PG, Sørensen JD, Thöns S. Information value-based optimization of structural and environmental monitoring for offshore wind turbines support structures.

Renew Energy. 2020;159:1036-1046. https://doi.org/10.1016/j.renene.2020.06.038

12. Farrar CR, Worden K. Structural health monitoring: a machine learning perspective. *Struct Heal Monit A Mach Learn Perspect*. New Jersey, US: John Wiley & Sons; 2012. https://doi.org/10.1002/9781118443118
13. Jacob A, Mehmanparast A, D'Urzo R, Kelleher J. Experimental and numerical investigation of residual stress effects on fatigue crack growth behaviour of S355 steel weldments. *Int J Fatigue*. 2019;128:105196. https://doi.org/10.1016/j.ijfatigue.2019.105196
14. Marco C, Paolo F, Filippo B, Giovanni M. Rapid calculation of residual notch stress intensity factors (R-NSIFs) by means of the peak stress method. *Intechopen*. 2020;1-15.
15. Ferro P, Berto F, James MN. Asymptotic residual stresses in butt-welded joints under fatigue loading. *Theor Appl Fract Mech*. 2016;83:114-124. https://doi.org/10.1016/j.tafmec.2016.02.002
16. Igwemezie V, Mehmanparast A, Brennan F. The role of microstructure in the corrosion-fatigue crack growth behaviour in structural steels. *Mater Sci Eng A*. 2020;803:140470. https://doi.org/10.1016/j.msea.2020.140470
17. Igwemezie V, Mehmanparast A. Waveform and frequency effects on corrosion-fatigue crack growth behaviour in modern marine steels. *Int J Fatigue*. 2020;134:105484. https://doi.org/10.1016/j.ijfatigue.2020.105484
18. Taylor J, Mehmanparast A, Kulka R, Moore P, Xu L, Farrahi GH. Experimental study of the relationship between fracture initiation toughness and brittle crack arrest toughness predicted from small-scale testing. *Theor Appl Fract Mech*. 2020;110;102799. https://doi.org/10.1016/j.tafmec.2020.102799
19. Mehmanparast A, Brennan F, Tavares I. Fatigue crack growth rates for offshore wind monopile weldments in air and seawater: SLIC inter-laboratory test results. *Mater Des*. 2017;494-504. https://doi.org/10.1016/j.matdes.2016.10.070
20. Mehmanparast A, Taylor J, Brennan F, Tavares I. Experimental investigation of mechanical and fracture properties of offshore wind monopile weldments: SLIC interlaboratory test results. *Fatigue Fract Eng Mater Struct*. 2018;41:2485-2501. https://doi.org/10.1111/ffe.12850
21. Hemmesi K, Farajian M. Numerical welding simulation as a basis for structural integrity assessment of structures: microstructure and residual stresses. *Dermatol Int*. Online: intechopen; 2018.
22. Zhu SP, Huang HZ, Ontiveros V, He LP, Modarres M. Probabilistic low cycle fatigue life prediction using an energy-based damage parameter and accounting for model uncertainty. *Int J Damage Mech*. 2012;21:1128-1153. https://doi.org/10.1177/1056789511429836
23. Fatemi A. Socie DF. A critical plane approach to multiaxial fatigue damage including out-of-phase loading. *Fatigue Fract Eng Mater Struct*. 1988;11:149-165. https://doi.org/10.1111/j.1460-2695.1988.tb01169.x
24. Correia J, Apetre N, Arcari A, et al. Generalized probabilistic model allowing for various fatigue damage variables. *Int J Fatigue*. 2017;100:187-194. https://doi.org/10.1016/j.ijfatigue.2017.03.031
25. Arany L, Bhattacharya S, Macdonald J, Hogan SJ. Design of monopiles for offshore wind turbines in 10 steps. *Soil Dyn Earthq Eng*. 2017;92:126-152. https://doi.org/10.1016/j.soildyn.2016.09.024
26. Biswal R, Mehmanparast A. Fatigue damage analysis of offshore wind turbine monopile weldments. *Procedia Struct Integr*. 2019;643-650. https://doi.org/10.1016/j.prostr.2019.08.086
27. Bocher M, Mehmanparast A, Braithwaite J, Shafiee M. New shape function solutions for fracture mechanics analysis of offshore wind turbine monopile foundations. *Ocean Eng*. 2018;160:264-275. https://doi.org/10.1016/j.oceaneng.2018.04.073
28. Kolios A, Wang L, Mehmanparast A, Brennan F. Determination of stress concentration factors in offshore wind welded structures through a hybrid experimental and numerical approach. *Ocean Eng*. 2019;178:38-47. https://doi.org/10.1016/j.oceaneng.2019.02.073
29. Jacob A, Oliveira J, Mehmanparast A, Hosseinzadeh F, Kelleher J, Berto F. Residual stress measurements in offshore wind monopile weldments using neutron diffraction technique and contour method. *Theor Appl Fract Mech*. 2018;418-427. https://doi.org/10.1016/j.tafmec.2018.06.001
30. Yeter B, Garbatov Y, Guedes Soares C. Numerical and experimental study of the ultimate strength of a monopile structure. *Eng Struct*. 2019;194:290-299. https://doi.org/10.1016/j.engstruct.2019.05.074
31. Mai QA, Weijtjens W, Devriendt C, Morato PG, Rigo P, Sørensen JD. Prediction of remaining fatigue life of welded joints in wind turbine support structures considering strain measurement and a joint distribution of oceanographic data. *Mar Struct*. 2019;66:307-322. https://doi.org/10.1016/j.marstruc.2019.05.002
32. Ambühl S, Kofoed JP, Sørensen JD. Determination of wave model uncertainties used for probabilistic reliability assessments of wave energy devices. *Proc Int Offshore Polar Eng Conf*. 2014;2:508-515.
33. Moghaddam BT, Hamedany AM, Taylor J, et al. Structural integrity assessment of floating offshore wind turbine support structures. *Ocean Eng*. 2020;208:107487. https://doi.org/10.1016/j.oceaneng.2020.107487
34. Igwemezie V, Mehmanparast A, Kolios A. Materials selection for XL wind turbine support structures: a corrosion-fatigue perspective. *Mar Struct*. 2018;381-397. https://doi.org/10.1016/j.marstruc.2018.06.008
35. Modulus T, Modulus C, Rates S. Strain-controlled fatigue testing 1. *ASTM Stand E606*. 2013;92:1-16. https://doi.org/10.1520/E0606-04E01.Copyright
36. Zhao D, Han N, Goh E, Cater J, Reinecke A. Offshore wind turbine aerodynamics modelling and measurements. *Wind Turbines Aerodyn Energy Harvest*. 2019;373-400. https://doi.org/10.1016/b978-0-12-817135-6.00005-3
37. ASTM E1049. Standard practices for cycle counting in fatigue analysis. *ASTM Stand*. 2017;85:1-10. https://doi.org/10.1520/E1049-85R17.2
38. Hansen MO. *Chapter 6: the classical blade element momentum method*. 3rd ed. Taylor Francis Group; 2015. https://doi.org/10.1049/ip-a-1.1983.0080
39. Models for metals subjected to cyclic loading. Abaqus Anal. User's Guid., vol. 6.14. In: *Dassault Systèmes*; 2014.
40. Norske Veritas D. RECOMMENDED PRACTICE DET NORSKE VERITAS AS Fatigue Design of Offshore Steel Structure. 2011.

How to cite this article: Biswal R, Al Mamun A, Mehmanparast A. On the performance of monopile weldments under service loading conditions and fatigue damage prediction. *Fatigue Fract Eng Mater Struct*. 2021;44:1469–1483. https://doi.org/10.1111/ffe.13442